PNAS RESEARCH ARTICLE | EARTH, ATMOSPHERIC, AND PLANETARY SCIENCES

Beyond spreading rate: Controls on the thermal regime of mid-ocean ridges

Jie Chen[a,1], Jean-Arthur Olive[b], and Mathilde Cannat[a]

Edited by Charles Langmuir, Harvard University, Cambridge, MA; received April 21, 2023; accepted September 20, 2023

The thermal state of mid-ocean ridges exerts a crucial modulation on seafloor spreading processes that shape ~2/3 of our planet's surface. Standard thermal models treat the ridge axis as a steady-state boundary layer between the hydrosphere and asthenosphere, whose thermal structure primarily reflects the local spreading rate. This framework explains the deepening of axial melt lenses (AMLs)—a proxy for the basaltic solidus isotherm—from ~1 to ~3 km from fast- to intermediate-spreading ridges but fails to account for shallow crustal AMLs documented at slow-ultraslow spreading ridges. Here, we show that these can be explained by a numerical model that decouples the potentially transient ridge magma supply from spreading rate, captures the essential physics of hydrothermal convection, and considers multiple modes of melt emplacement. Our simulations show that melt flux is a better thermal predictor than spreading rate. While multiple combinations of melt/dike emplacement modes, permeability structure, and temporal fluctuations of melt supply can explain shallow crustal AMLs at slow-ultraslow ridges, they all require elevated melt fluxes compared to most ridge sections of comparable spreading rates. This highlights the importance of along-axis melt focusing at slow-ultraslow ridges and sheds light on the natural variability of their thermal regimes.

mid-ocean ridges | thermal regime | melt flux | melt emplacement | hydrothermal circulation

Significance

We demonstrate that the spreading rate alone is a poor indicator of the thermal state of slow–ultraslow spreading mid-ocean ridges (MORs). Our numerical models, coupling hydrothermal convection with transient magmatic intrusions, show that melt flux, not spreading rate, is the primary control on the depth of axial melt lenses (AMLs), a strong proxy for the thermal state. For slow-ultraslow spreading ridges that account for 2/3 of the global MOR length, the mode of melt emplacement and the transience of the magma are crucial thermal controls. The AML depth at slow–ultraslow spreading ridges can fluctuate through time as magma supply waxes and wanes, and a shallow AML (2–4 km) can only form during an inherently ephemeral phase of elevated melt fluxes.

The strength of young oceanic lithosphere is largely influenced by the thermal regime of mid-ocean ridges (MORs) (1–3), which is shaped by a dynamic balance between heat supplied by magma cooling and crystallization, and heat lost through hydrothermal circulation (4–7). Seismically imaged axial melt lenses (AMLs) and/or low P wave velocity anomalies (LVAs) are strong indicators of the thermal structure of MORs, as they constitute proxies for the basaltic solidus (~1,000 °C) that encloses crystal mush zones at the ridge axis (Fig. 1 *A* and *B*) (4, 8, 9). Standard thermal models (4, 5) predict MOR thermal regimes that dramatically cool as the full spreading rate decreases below 60 km/My, such that a steady-state AML cannot exist within the crust at spreading rates below ~40 km/My (Fig. 1*C*). These models assume a global average thickness of 6 km for the magmatic crust and treat hydrothermal circulation as either diffusion enhanced by a multiplying factor referred to as the Nusselt number (4) or a porous convection system (5). Their predicted solidus isotherms fit well with AML/LVA depths observed at fast and most intermediate spreading ridges (Fig. 1*C*) (4, 5, 10). However, at slow–ultraslow spreading ridges, which account for over two-thirds of the global MOR, standard models that assume a steady-state system fail to explain the presence of shallow crustal AMLs/LVAs (2–4 km below the seafloor) at the centers of certain magmatically robust segments (Figs. 1 and 2*A*) (11–19). Besides, the depth of microseismic events in many slow–ultraslow ridge sections reaches 10–15 km (20–22), suggesting that the brittle-ductile transition, and therefore the solidus isotherm should lie below the crust if magma supply were indeed steady through time (e.g., Fig. 2*B*).

To better understand MOR thermal regimes, we evaluate multiple controls beyond spreading rate, by performing 2-D numerical simulations (7, 26, 27) that couple asthenosphere upwelling, shallow hydrothermal convection in the lithosphere, and repeated melt intrusions (Fig. 2*C*; *Methods*). The magma supply is partitioned between repeated horizontal AML injections of specified extent, emplaced just below the basaltic solidus isotherm, and vertical dike intrusions connecting the solidus and the seafloor. The frequency of dike intrusions is set so that through time, they accommodate a fraction (F_{dike}) of the plate divergence in the crust (*Methods*). Hydrothermal convection is confined above a maximum depth of 2.5 to 5 km, within a permeable layer with permeability ranging between 5×10^{-16} and 1×10^{-15} m^2. We first calibrate our simulations to reproduce AML depths predicted by standard models of fast-intermediate spreading ridges (Figs. 2*D* and 3*A*, and *SI Appendix*, Fig. S2). This is achieved by assuming a 6-km-thick magmatic crust and $F_{dike} = 1$ (the best fit is obtained for a hydrothermal system confined to a maximum depth of 5 km, and a

Author affiliations: [a]Institut de Physique du Globe de Paris, Université Paris Cité, CNRS, Paris 75005, France; and [b]Laboratoire de Géologie, CNRS - Ecole Normale Supérieure - L'université Paris Sciences & Lettres, Paris 75005, France

Author contributions: J.C., J.-A.O., and M.C. designed research; J.-A.O. and M.C. provided comments and revisions throughout the work; and J.C. performed the numerical modeling and wrote the paper.

The authors declare no competing interest.

This article is a PNAS Direct Submission.

[1]To whom correspondence may be addressed. Email: chenjie.geo@outlook.com.

This article contains supporting information online at https://www.pnas.org/lookup/suppl/doi:10.1073/pnas.2306466120/-/DCSupplemental.

Published October 30, 2023.

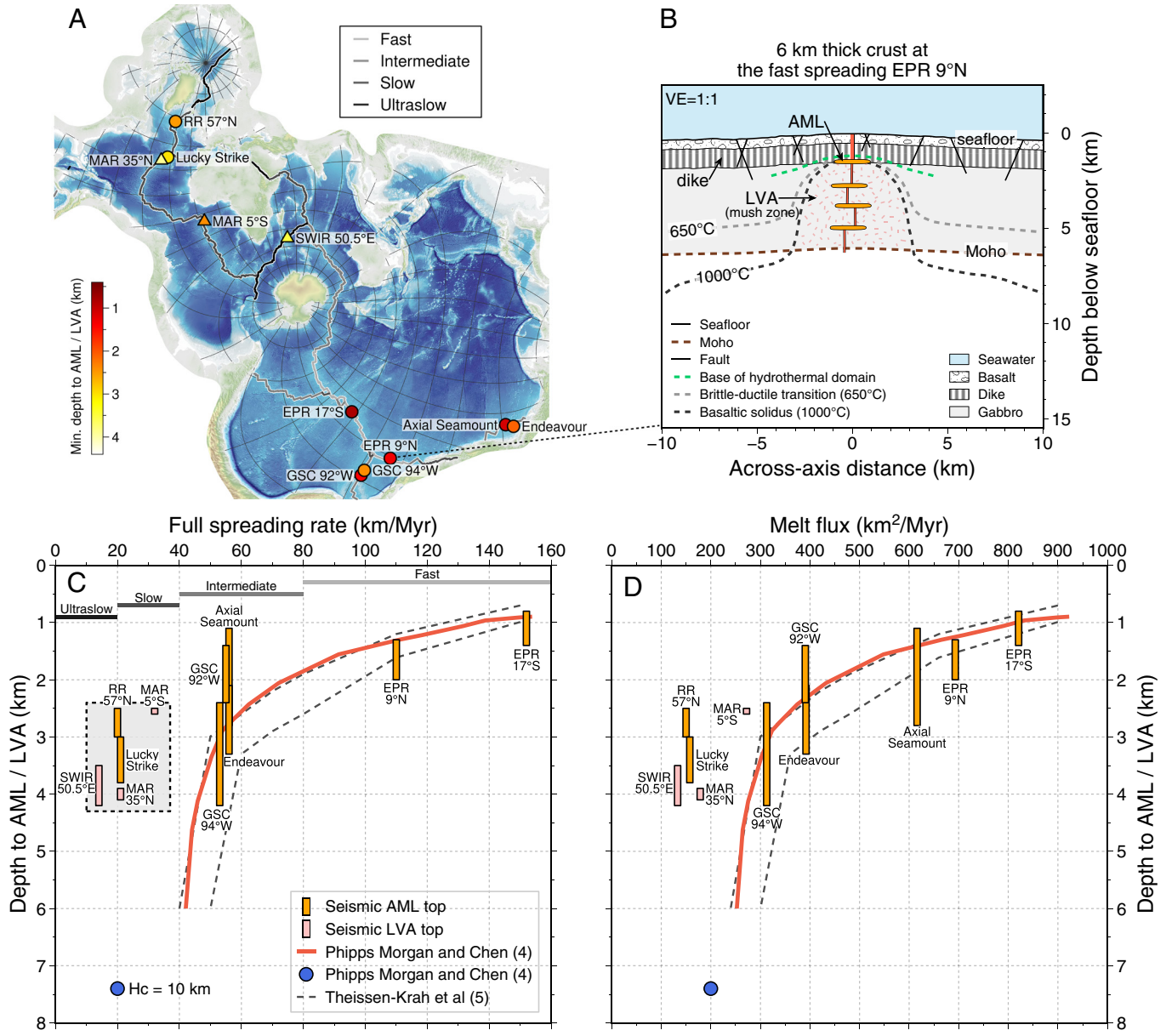

Fig. 1. Seismic observations of AMLs/LVAs at mid-ocean ridges vs. standard thermal models. (*A*) Spilhaus square projection map (23) showing the world's oceans, as well as fast (>80 mm/y), intermediate (40–80 mm/y), slow (20–40 mm/y), and ultraslow (<20 mm/y) spreading ridges. Filled circles and triangles represent the shallowest depth of seismically imaged axial melt lenses (AMLs) and low P wave velocity anomalies (LVAs), respectively. (*B*) Schematic cross-section of the fast-spreading EPR 9°N (modified from refs. 9 and 10). (*C*) Depth to the AML/LVA vs. spreading rate, predicted by the Nusselt (*Nu*) parameterization (4) (red line for $Nu = 8$), and a 2-D hydrothermal convection model (5) with permeabilities of 4 and 6×10^{-15} m^2 (upper and lower dash lines, respectively). Magmatic crustal thickness is assumed to be the global average value of $Hc = 6$ km, except for the blue circle ($Hc = 10$ km). Hydrothermal domains are all confined above 6 km with a cut-off temperature of 600 °C. (*D*) AML/LVA depth vs. melt flux (spreading rate times crustal thickness). Depths to seismically determined AMLs (orange rectangles) and LVAs (pink rectangles), as well as crustal thicknesses (for calculating melt fluxes) included are 17°S and 9°N of the East Pacific Rise (EPR), Axial Seamount and Endeavor of the Juan de Fuca Ridge (JdFR), 92°W and 94°W of the Galapagos Spreading Center (GSC), Lucky Strike, 35°N, and 5°S of the Mid-Atlantic Ridge (MAR), 57°N of the Reykjanes Ridge (RR), and 50.5°E of the Southwest Indian Ridge (SWIR). Data and references are listed in *SI Appendix*, Table S1.

permeability of 1×10^{-15} m^2). This calibrated model then enables us to systematically explore the following thermal controls: 1) melt flux (φ; Fig. 3): the product of spreading rate (U) and crustal thickness (Hc), 2) dike-accommodated fraction of plate separation in the crust (F_{dike}; Fig. 3), 3) the maximum potential depth extent (Z_{H0}) and the permeability (k) of the hydrothermal system (Fig. 4), and 4) cyclic fluctuations in melt supply about an average flux defined by the time-integrated crustal thickness (Fig. 5).

Melt Flux Instead of Spreading Rate. Melt flux (φ) at the MOR is highly variable and decoupled from the spreading rate at slow-ultraslow spreading ridges (25, 29). This is particularly evident at ultraslow spreading ridges such as the SWIR, whose melt supply can be nearly zero at 64.5°E (30) while a 9.5-km-thick magmatic crust accretes at 50.5°E with a similar spreading rate (14). We thus reassess observed AML/LVA depths as a function of melt flux instead of spreading rate (Fig. 1*D*). This improves the fit between seismic observations and numerical predictions, particularly at the Axial Seamount section of the intermediate-spreading Juan de Fuca Ridge, which has a high melt flux (616 km^2/My) due to an unusually thick crust (11 km) (31).

To simulate a ridge with an elevated magma input, we run a suite of simulations with $Hc = 7.5$, 9.5, and 11 km, corresponding to crustal thicknesses measured at the Lucky Strike segment of the

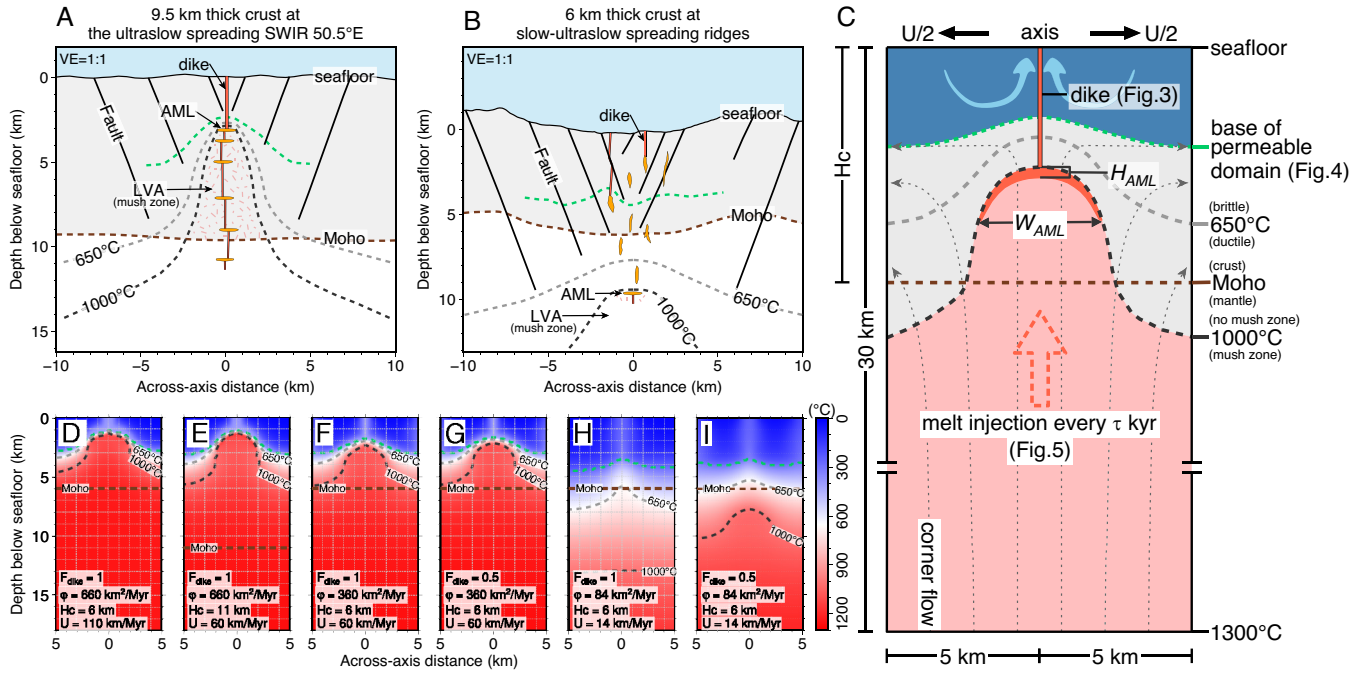

Fig. 2. Schematic cross-sections of slow-ultraslow spreading ridges and the thermal model of this study. (*A*) Cross-section of the magmatically robust SWIR 50.5°E segment with a 9.5 km-thick crust and a crustal LVA (modified from ref. 24). (*B*) Cross-section of a less magmatic slow–ultraslow spreading segment with a 6-km-thick crust (modified from ref. 2). (*C*) Cartoon of the thermal model setup (modified from ref. 25). (*D–I*) Model snapshots of steady-state thermal regimes. Key model parameters are listed at the bottom. Hydrothermal domains are all confined above Z_{H0} = 5 km with a permeability of $k = 1 \times 10^{-15}$ m^2. Dashed green, gray, black, and brown lines represent the base of the permeable domain, the 650 °C and 1,000 °C isotherms, and the Moho, respectively. (*D*) Case representing the fast-spreading EPR 9°N. (*E*) Case representative of a magmatically robust intermediate spreading ridge (e.g., Axial Seamount) with the same melt flux as EPR 9°N, showing the same AML depth as EPR 9°N but a colder thermal regime beneath the solidus. (*F* and *G*) Cases representative of intermediate spreading ridges with a 6-km-thick crust at F_{dike} = 1 and 0.5, respectively, showing the small effect of F_{dike} on the thermal regime of intermediate spreading ridges. (*H* and *I*) Cases representative of ultraslow spreading ridges with a 6-km-thick crust at F_{dike} = 1 and 0.5, respectively. In the simulation with F_{dike} = 1, all melts are treated as dike intrusions that cut through the entire crust, but no AML is emplaced beneath the solidus as it lies below the crust, which may produce an unrealistic thermal regime. In the simulation with F_{dike} = 0.5, AMLs are still emplaced beneath the solidus and crystallize in the mantle but not in the crust, while dikes only lie at crustal depths with no connections to AMLs. *U*: spreading rate. *Hc*: equivalent magmatic (crustal) thickness. φ: melt flux. F_{dike}: dike-accommodated fraction of plate separation in the crust. 650 °C and 1,000 °C isotherms: brittle-ductile transition and basaltic solidus. W_{AML}: AML width. H_{AML}: AML thickness. τ: time interval of melt injections. See more model parameters in *SI Appendix*, Table S2.

Mid-Atlantic Ridge (19) and the 57°N segment of the RR (16), the 50.5°E segment of the SWIR (14), and Axial Seamount (31), respectively (Fig. 3*A*). These models yield AML depths that are all deeper than those imaged through seismic observations at magmatically robust slow–ultraslow spreading segments (Fig. 3*A*). This discrepancy is also present when assuming a thicker crust in the standard model (4), as demonstrated by the case with *U* = 20 km/My and *Hc* = 10 km shown as a blue circle in Fig. 1*C*. This simple approach thus cannot explain the shallow crustal AMLs/LVAs at slow–ultraslow spreading ridges.

In Fig. 3*B*, predicted AML depths are plotted against melt flux for simulations with *Hc* = 6 and 11 km. This plot shows that for melt fluxes in excess of ~400 km^2/My (the melt flux of a 67 km/My, intermediate spreading ridge with *Hc* = 6 km), the two curves overlap (Fig. 3*B*). This suggests that the axial thermal regime of fast and intermediate spreading ridges also primarily reflects the elevated melt flux as opposed to spreading rate (e.g., Axial Seamount in Fig. 2*E*). For melt fluxes decreasing below ~400 km^2/My, the two curves increasingly diverge, and for a given melt flux, a thinner crust (i.e., a faster spreading rate) produces a colder thermal regime. This is because after filling the crustal dike to accommodate plate separation, there is less melt available to fill the mush zone in simulations with *Hc* = 6 km, compared to simulations with *Hc* = 11 km (*Methods*). Proportionally more melt is thus emplaced at shallow depths (i.e., close to the hydrothermal system) in simulations with *Hc* = 6 km, allowing more efficient hydrothermal heat extraction to cool the thermal regime (27). This highlights the critical control of the modes of melt emplacement on the thermal regime of slow–ultraslow spreading ridges for a given melt flux.

Modes of Magma Emplacement. Plate separation at MORs is accommodated by melt intrusions and faults (1, 3); the dike-accommodated fraction of extension (F_{dike}) in the upper crust of fast ridges is nearly uniformly 1 with very few faults (Fig. 1*B*) (32, 33), while F_{dike} is more variable at slow–ultraslow ridges, where faults can accommodate 10–100% of plate divergence (i.e., F_{dike} = 0.9–0) (28, 30, 34). Standard models assume that the upper crust is built by dike intrusions that accommodate 100% of the plate spreading at all spreading rates, while the lower crust is emplaced through downward and outward crustal flows from a shallow AML (4, 5, 24, 35). This assumption overestimates the heat supplied through dike intrusions to the upper crust of slow–ultraslow ridges, resulting in hydrothermal heat removal that is too efficient and, thus, colder thermal regimes than in reality. Unrealistically, when the solidus isotherm lies beneath the crust (e.g., Fig. 2*H*), standard models treat all melt emplacement as dike intrusions with no associated AML (i.e., the entire crust is built by dikes). This explains why they do not predict AMLs deeper than 6 km at spreading rates below 40 km/My (Fig. 2*H* for the case of *U* = 14 km/My).

Parameterizing dike emplacement through a variable F_{dike} (from 1 to 0) enables our model to simulate the thermal regime at all possible spreading rates and crustal thicknesses (*Methods*). Changing F_{dike} has hardly any effect on fast and intermediate spreading ridges (Fig. 3*C*). At slow–ultraslow ridges, however, for

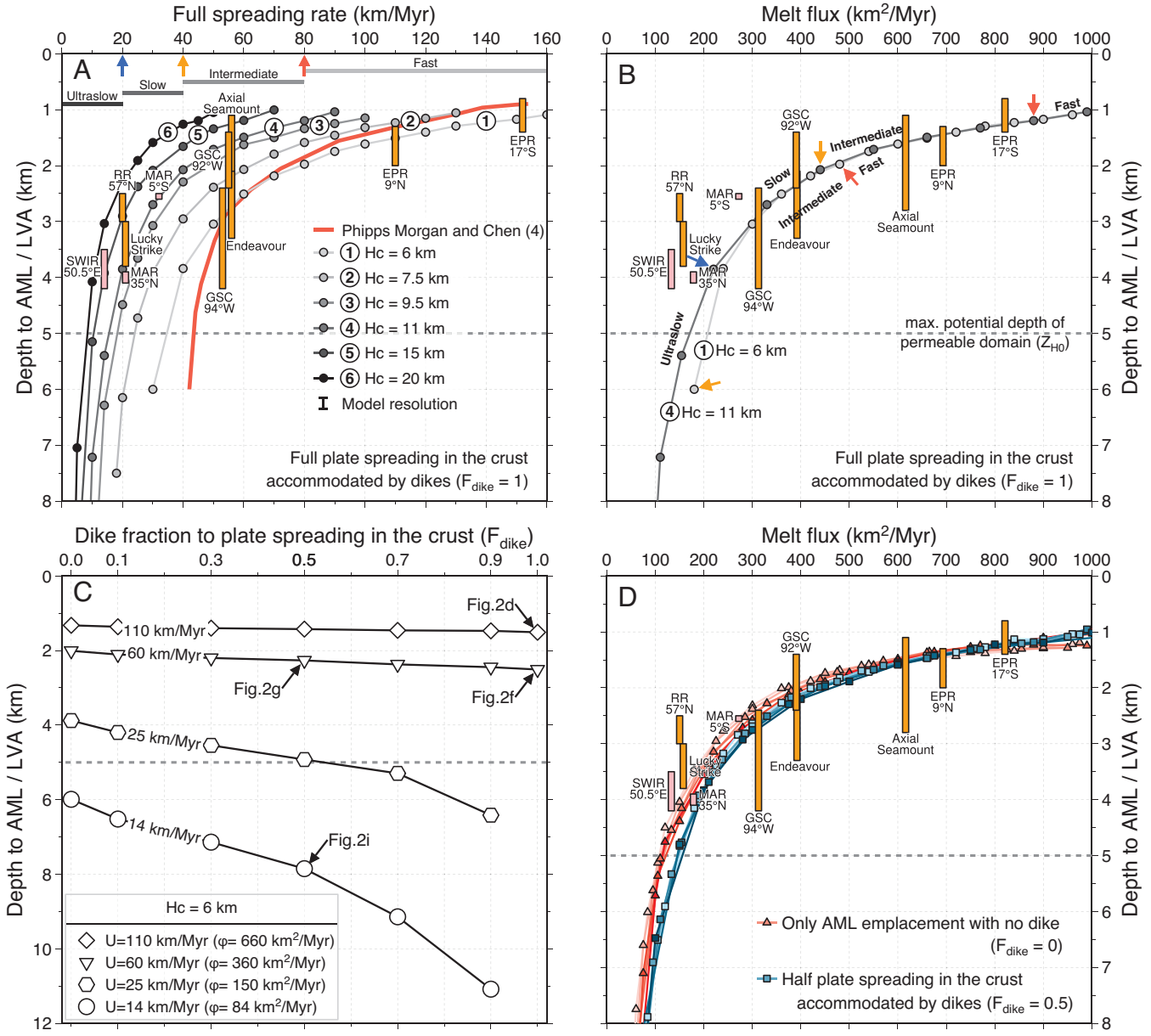

Fig. 3. Thermal effects of spreading rate, melt flux, and the dike-accommodated fraction of the plate spreading in the crust (F_{dike}). Hydrothermal domains are all confined above Z_{H0} = 5 km with a permeability of $k = 1 \times 10^{-15}$ m^2. All depths are measured ±0.1 km, which corresponds to the grid size. (*A*) AML depth vs. spreading rate. Red line is predicted by the Nusselt parameterization with *Hc* = 6 km (4). Six groups of simulations (numerical labels) are run with crustal thicknesses of *Hc* = 6, 7.5, 9.5, 11, 15, and 20 km. Full plate spreading in the crust is accommodated by dikes (F_{dike} = 1). (*B*) AML depth vs. melt flux for simulations with *Hc* = 6 and 11 km in *A*. Note that the combination of spreading rate and crustal thickness can be different for the same melt flux. Blue, orange, and red arrows represent boundaries of ultraslow–slow, slow–intermediate, and intermediate–fast spreading ridges, respectively. (*C*) AML depth vs. F_{dike} for simulations of *U* = 110, 60, 25, and 14 km/My with a constant *Hc* = 6 km, representing fast, intermediate, slow, and ultraslow spreading ridges, respectively. (*D*) AML depth vs. melt flux for simulations of only AML emplacement with no dike (F_{dike} = 0) and half plate spreading in the crust accommodated by dikes (F_{dike} = 0.5). Six groups of simulations are run with the same configuration of *U* and *Hc* as simulations of F_{dike} = 1 (*A*). See *SI Appendix*, Fig. S5 *A* and *B* for the plots of AML depth vs. spreading rate at F_{dike} = 0 and F_{dike} = 0.5, respectively.

a given spreading rate and crustal thickness, a lower F_{dike} corresponds to a lower fraction of the magmatic input feeding dike intrusions and thus a greater proportion feeding AML emplacements, causing a hotter thermal regime (Fig. 3*C*). For example, at *U* = 25 km/My and Hc = 6 km, crustal AMLs only exist for F_{dike} < ~0.8. More strikingly, at *U* = 14 km/My and Hc = 6 km, the AML deepens from 6 to 11 km from F_{dike} = 0 to 0.9 (Fig. 2*I* for the case of F_{dike} = 0.5).

To further explore this idea, we run two groups of simulations with F_{dike} = 0 (the melt is only emplaced as AMLs; Fig. 3*D* and *SI Appendix*, Fig. S5*A*) and F_{dike} = 0.5 (the amount of melt emplaced in dikes suffices to accommodate half of the plate divergence in the crust, and the remainder of the melt flux is emplaced as AMLs; Fig. 3*D* and *SI Appendix*, Fig. S5*B*), using the same combinations of spreading rate and crustal thickness (i.e., melt flux conditions) as in simulations with F_{dike} = 1 (Fig. 3*A*). In these simulations, proportionally more melt is emplaced in the AML for any combination of *Hc* and *U*, resulting in hotter thermal regimes and shallower predictions for AML/LVA depths at slow–ultraslow spreading rates, than simulations with F_{dike} = 1. All predictions of AML depths at a given F_{dike} collapse onto a single curve when plotted against melt flux (Fig. 3*D*), suggesting that the thermal regime at $F_{dike} \leq 0.5$ depends entirely on magma supply rather than spreading rate. However, even with F_{dike} = 0, these

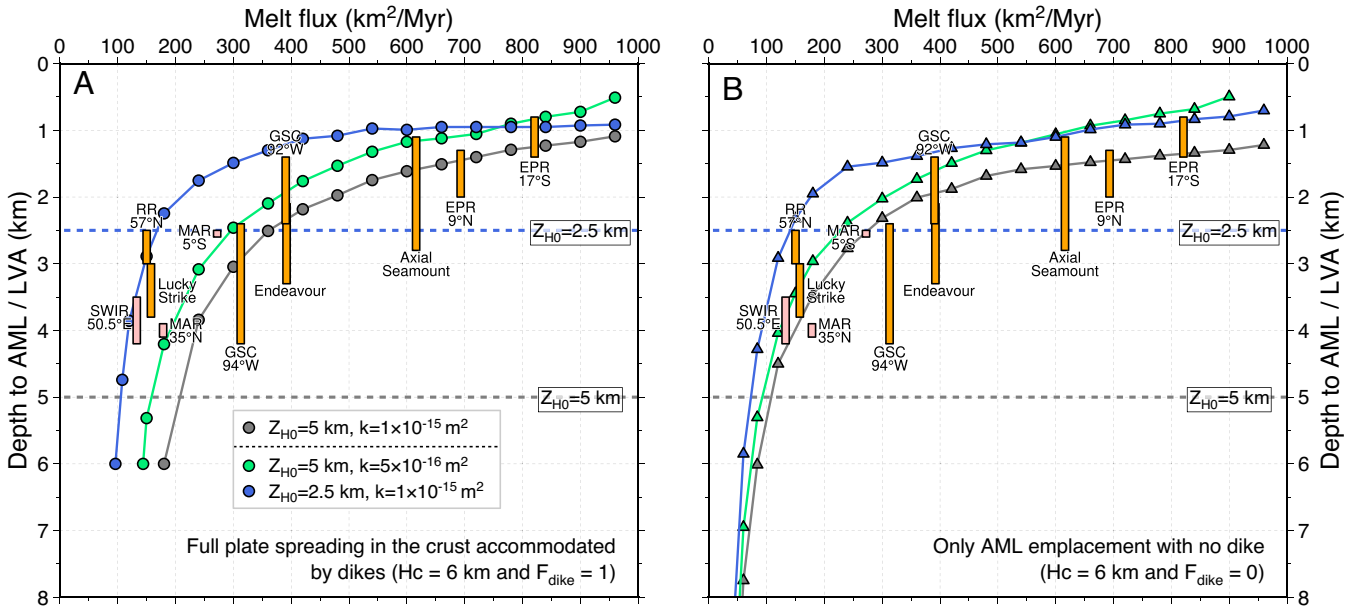

Fig. 4. Thermal effects of the maximum potential depth extent (Z_{H0}) and the permeability (k) of the hydrothermal system. See legend for combinations of Z_{H0} and k. Simulations with Z_{H0} = 5 km and k = 1 × 10^{-15} m^2 are taken as references. All simulations are run with a constant crustal thickness Hc = 6 km. (*A*) F_{dike} = 1. (*B*) F_{dike} = 0. See *SI Appendix*, Fig. S5*C* for F_{dike} = 0.5.

predictions fall short of explaining the AML/LVA depths at centers of magmatically robust segments of slow–ultraslow ridges (i.e., RR-57°N, Lucky Strike, and, to a lesser extent SWIR-50.5°E, Fig. 3*D*). In addition, F_{dike} could actually be >0.9 at these magmatically robust sites, as can be inferred from the tectonic fraction of extension estimated from summing fault offsets in high-resolution bathymetry maps (28, 36). A low fraction of melt emplaced as dikes is thus not a satisfactory explanation for these AMLs/LVAs bearing slow–ultraslow ridge sections.

Permeability and Maximum Allowed Depth Extent of the Hydrothermal System. The third family of parameters we investigate pertains to the efficiency of heat extraction by the hydrothermal convective system. This efficiency is reduced in more shallowly confined systems (shallower Z_{H0}) (7, 27) with lower permeability (k) (5, 26, 27, 37). Here, we use simulations with Z_{H0} = 5 km and k = 1 × 10^{-15} m^2 as references (using F_{dike} = 1, 0.5, and 0 with a constant Hc = 6 km) and run simulations with a shallower Z_{H0} (2.5 km) and a lower permeability (5 × 10^{-16}

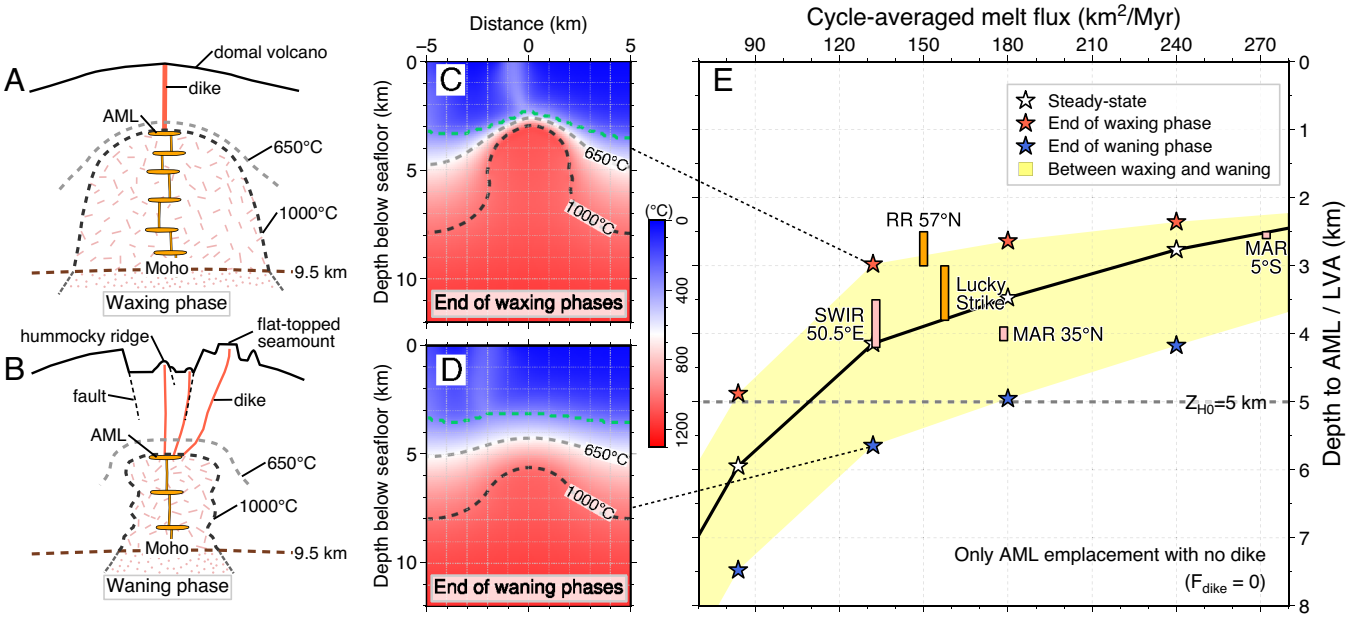

Fig. 5. Thermal effects of cyclic changes in melt supply. (*A* and *B*) Schematic cross sections corresponding to waxing and waning phases of a fluctuating magma supply at 50.5°E on the SWIR (modified from ref. 24), respectively. (*C* and *D*) Snapshots of thermal regimes at the ends of waxing and waning phases, respectively, for key models, whose parameters are adjusted to the SWIR 50.5°E (27). Dashed green, gray, and black lines represent the base of the permeable domain, the 650 °C isotherm, and 1,000 °C isotherm, respectively. (*E*) Predicted range of AML depths in the cyclic melt supply with melt fluxes covering slow–ultraslow spreading ridges. The cycle duration is 300 kyr based on geological observations at the SWIR 50.5°E (28). Melt fluxes at waxing and waning phases are set to 2 and 0.5 times the average for 100- and 200-kyr durations, respectively. This configuration produces the broadest range of AML depths. See *SI Appendix*, Fig. S6 for time series of the AML depth change and for the cyclic melt supply with the smallest range of AML depths. Only AMLs are emplaced with no dike (F_{dike} = 0) in all simulations of cyclic melt supply. Hydrothermal domains are confined above Z_{H0} = 5 km with a permeability of k = 1 × 10^{-15} m^2.

m^2). This shifts the depths of predicted AMLs upward (Fig. 4 and *SI Appendix*, Fig. S5*C*), to depths that are shallower than most observed AMLs. These runs successfully predict shallow AMLs for slow–ultraslow ridges (Fig. 4), yet there is no evidence that hydrothermal systems there are confined to the uppermost crust nor that this uppermost crust has such a low permeability (38). In fact, microearthquakes interpreted as related to hydrothermal cooling above the Lucky Strike AML occur down to 3–3.5 km below the seafloor (39), suggesting that hydrothermal fluids penetrate to at least that depth.

Cyclic Changes in Melt Supply. The last thermal control explored is cyclic changes in melt supply over time scales that are commensurate to, or shorter, than the time it takes to form a new crust in the axial domain. Such cyclic changes have been documented at several slow–ultraslow ridge sections (28, 40–42). Geological observations at SWIR-50.5°E indicate a 300-ky cycle with alternating waxing and waning phases of melt supply (28), and a cycle-averaged melt flux of 133 km^2/My is constrained by the geophysically determined crustal thickness (43) (9.5 km) and the spreading rate (14 km/My) (44). These cycles could be caused by thermo-chemical heterogeneities in the subridge mantle that modulate magma production and/or by the dynamics of magma transport and collection to the axis, which can be highly unsteady and wave-like (41, 42, 45). This ridge section is currently in what is interpreted as an intermediate stage from waxing to waning (Fig. 5 *A* and *B*) (28). The current LVA depth at SWIR-50.5°E is successfully bracketed (Fig. 5 *C*–*E*) by runs with the inferred cycle-averaged melt flux, F_{dike} = 0 (i.e., the hottest parameter configuration), Z_{H0} = 5 km, $k = 1 \times 10^{-15}$ m^2, and waxing and waning phases with fluxes of 2/0.5 times the cycle average, lasting 100 and 200 ky, respectively (27). Extending this approach to the appropriate range of melt fluxes, we model AML depths that successfully bracket all but one (RR-57°N; Fig. 5*E*) seismically imaged AMLs/LVAs documented at slow–ultraslow spreading ridges. In the runs, the shallowest and deepest AMLs correspond to the ends of waxing and waning phases, respectively (Fig. 5 *C* and *D*). The range of possible AML depths depends on respective melt fluxes and durations of waxing and waning phases, which has been explored in ref. 25. The values used here yield the broadest contrast between waxing and waning thermal configurations.

Discussion

In Fig. 6, we integrate end-member thermal predictions made in this study and plot them against spreading rate (Fig. 6*A*) and melt flux (Fig. 6*B*). Doing so highlights how melt flux is a better predictor of AML/LVA depths than spreading rate. It also shows that shallow crustal AMLs/LVAs detected at slow–ultraslow spreading ridges are predicted only in runs with cyclic melt supply, and/or less efficient hydrothermal cooling. While less efficient hydrothermal cooling might account for RR AML depths given the scarcity of hydrothermal signatures in that region (46, 47), it certainly cannot be invoked to explain the Lucky Strike AML that feeds one of the most vigorous Mid-Atlantic Ridge (MAR) hydrothermal vent fields (48). The hot thermal regime at RR-57°N, which is suspected to be in the waxing phase of a cyclic melt supply (17), might also be explained by its location over the edge of the Iceland mantle plume, with a mantle hotter than assumed in our models (49).

With the possible exception of this RR-57°N case, AML/LVA-bearing slow–ultraslow ridge sections are restricted to the center of segments, and their anomalously high melt supply is interpreted as the result of along-axis melt focusing (50–52). Similarly, transient crustal AMLs are likely occurring in other slow–ultraslow ridge segment centers, such as the Menez Gwen segment of the MAR (40) and the Joseph Mayes Seamount of the SWIR (53), although seismic surveys are required to validate these predictions. Broadly speaking, our results show how taking melt flux into account, and not just spreading rate, is necessary to explain the observed thermal regime of slow–ultraslow ridges. This also requires amendments to standard models (4, 5, 35) of steady and fully dike-accommodated crustal accretion at these ridges. We favor a model where melts can be emplaced transiently across a wide range of depths from near the seafloor to the deeper mush zone (e.g., Fig. 2*B*) (54). Accounting for multiple modes of emplacement in settings where the axial lithosphere is commonly thicker than the crust allows a great diversity of thermal regimes for a given melt flux (27). Our model also highlights the transient

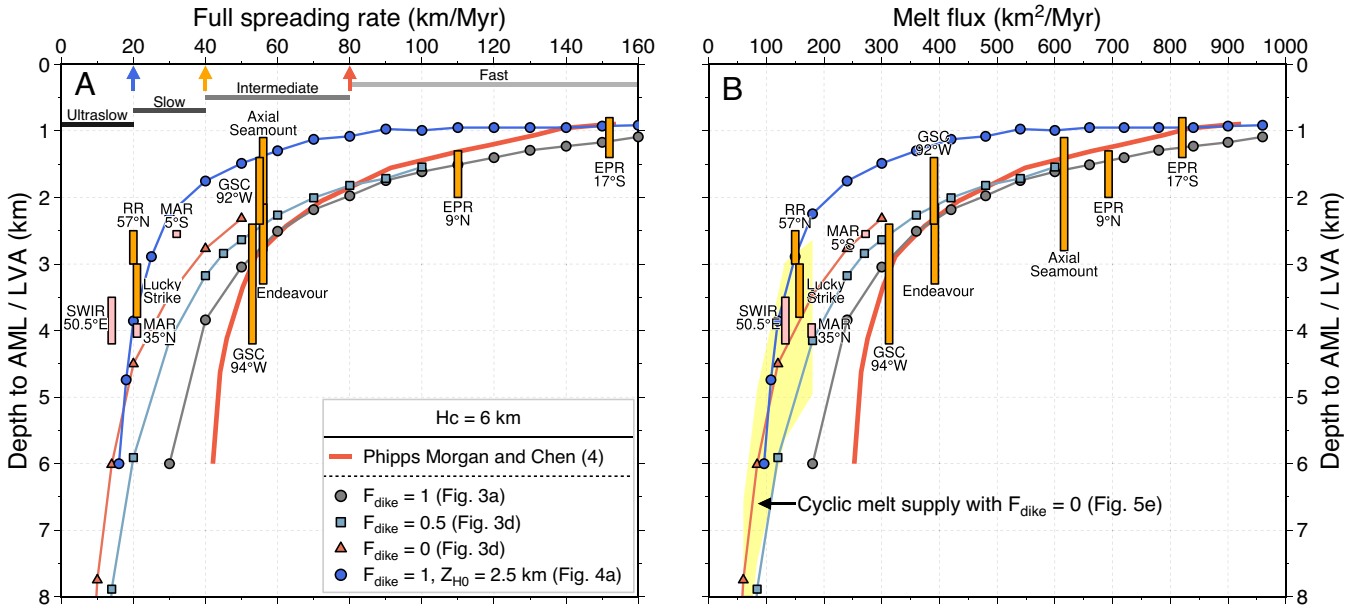

Fig. 6. Summary of plausible thermal regimes corresponding to a wide range of parameters. (*A*) AML depth vs. spreading rate. See legend for simulation parameter, which all use *Hc* = 6 km. (*B*) AML depth vs. melt flux. The range calculated for cyclic melt supply variations in Fig. 5*E* is shown in yellow.

nature of the thermal regime at extremely magmatic sections of slow–ultraslow ridge sections.

Methods

All numerical simulations were conducted with the MATLAB code *multiporo* (7, 26, 27), which is a 2-D porous convection model coupling hydrothermal circulation and magma injection (model parameters in *SI Appendix*, Table S2). The model setup is adopted from previous studies (26, 27). The numerical domain is 30 km high and 10 km wide and discretized as 100-m wide cells (Fig. 2*C*). The top boundary (i.e., seafloor) temperature (T_0) is set to 0 °C, and the bottom boundary temperature (T_b) is imposed at 1,300 °C. The basaltic solidus (T_S) and the liquidus (T_M) are set to 1,000 and 1,200 °C, respectively, based on the average composition of mid-ocean ridge basalts (8). The initial temperature field is set to linearly increase from 0 °C to 1,000 °C between the seafloor and 1.5 km depth and to linearly increase from 1,000 °C to 1,300 °C between 1.5 km and the bottom of the domain. Hydrothermal convection is modeled as Darcy porous flow and confined above the depth of a cracking front (Z_H; Fig. 2*C*). We parameterize the hydrothermal domain as a permeable domain with a uniform permeability (k) and a maximum potential depth extent that represent the deepest reach of a cracking front (Z_{H0}) (7, 26, 27). In the underlying, impermeable domain, heat can only be conducted, or advected by solid flow of the asthenosphere. We model mantle upwelling as a 2-D solid flow, which is assumed to develop as a response to the symmetric spreading of the overriding plates according to an analytical corner flow solution (55). The corner flow is only applied in the domain between the model bottom and the depth of the brittle-ductile transition (BDT, set to 650 °C) in the central profile (i.e., at ridge axis of $x = 0$; Fig. 2*C*). The thermal effect of assuming mantle (corner) flow up to the seafloor, the 400 °C isotherm, the 650 °C isotherm (our default assumption; corresponding to the base of the brittle lithosphere), the 1,000 °C isotherm (close to the base of the ductile lithosphere), or no corner flow at all is illustrated in *SI Appendix*, Fig. S4. It shows that this effect is negligible at fast-intermediate spreading ridges but more significant at slow–ultraslow spreading ridges, especially with $F_{dike} = 1$ (*SI Appendix*, Fig. S4*A*). All simulations, except for those with cyclic melt supply, were run until they reached steady-state thermal regimes.

AML Emplacement. In simulations without diking ($F_{dike} = 0$), AMLs are emplaced just below the solidus isotherm by resetting the temperature to T_M within a domain of horizontal and vertical extent W_{AML} and H_{AML}, respectively, every time interval τ_{AML}, such that repeated AML intrusions account for a total melt flux φ:

$$\varphi = U \cdot Hc = \frac{W_{AML} \cdot H_{AML}}{\tau_{AML}}. \quad [1]$$

In Eq. **1**, U and Hc are full spreading rate and equivalent magmatic (crustal) thickness of a ridge section, respectively. For example, the 50.5°E segment of the SWIR has an ultraslow spreading rate of $U = 14$ km/My and a crustal thickness of up to $Hc = 9.5$ km (13, 14), yielding a melt flux of $\varphi = 133$ km^2/My, which is equivalent to a slow spreading ridge with $U = \sim 22$ km/My and $Hc = 6$ km. As the shape of the AML plays a minor role in the axial thermal regime at a given melt flux (27), we fix $W_{AML} = 4$ km and $H_{AML} = 0.2$ km in all simulations with $F_{dike} = 0$. The melt flux, determined by spreading rate and crustal thickness, is thus only related to the time interval of melt injection (τ_{AML}) or the frequency of melt injection ($1/\tau_{AML}$; *SI Appendix*, Fig. S1). The emplaced AML is always centered in the horizontal direction ($x = 0$), and its top coincides with the solidus isotherm ($T_S = 1{,}000$ °C). The AML releases specific and latent heat upon cooling and crystallizing, respectively (6), and this heat fuels hydrothermal convection above the cracking front.

Dike Intrusion. Dikes are centered in the horizontal direction (i.e., at the ridge axis: $x = 0$), connecting the AML top (the solidus isotherm) with the seafloor, thereby building the upper crust. The remainder of the melt is emplaced beneath the solidus isotherm as AMLs, which build the lower crust. If the AML lies at crustal depths, the dike height (H_{dike}) is equal to the AML depth (Z_{AML}). The dike width (W_{dike}) is expressed as:

$$W_{dike} = F_{dike} \cdot (U \cdot \tau_{dike}), \quad [2]$$

where τ_{dike} is the time interval of dike intrusions, and F_{dike} is the dike-accommodated fraction of plate separation in the crust ($1 - F_{dike}$ can be thought of as the fault-accommodated fraction of plate separation).

At $F_{dike} = 0$, AML emplacements only occur beneath the solidus (see previous subsection). At $F_{dike} > 0$, melt fluxes for the upper crust φ_{UC} and the lower crust φ_{LC} are expressed as:

$$\varphi = \varphi_{UC} + \varphi_{LC}, \quad [3]$$

$$\varphi_{UC} = \frac{W_{dike} \cdot H_{dike}}{\tau_{dike}}, \quad [4]$$

$$\varphi_{LC} = \frac{W_{AML}' \cdot H_{AML}'}{\tau_{AML}'}, \quad [5]$$

where W_{AML}', H_{AML}', and τ_{AML}' are the width, thickness, and time interval of the AML emplacement in the lower crust, respectively. We fix:

$$W_{AML}' = W_{AML} = 4 \text{ km}. \quad [6]$$

We then simplify the dike intrusion and the AML emplacement to occur simultaneously, which yields the following equation:

$$\tau_{dike} = \tau_{AML}' = \tau_{AML} = \tau. \quad [7]$$

We also consider that the amount of melt at every injection (dike plus AML) is constant at $W_{AML} \cdot H_{AML}$ [1]. Combining [1] to [7], we get:

$$W_{AML} \cdot H_{AML} = W_{AML} \cdot H_{AML}' + F_{dike} \cdot (U \cdot \tau) \cdot H_{dike}, \quad [8]$$

where W_{AML} and H_{AML} are fixed, and τ can be calculated from U and Hc according to Eq. **1**. H_{dike} is measured as Z_{AML} if the AML lies at crustal depths, F_{dike} is a parameter to be chosen, and H_{AML}' can be calculated once F_{dike} is given.

Combining [1] and [8], proportions of melt flux for the upper crust (P_{UC}) and the lower crust (P_{LC}) can be expressed as:

$$P_{UC} = \frac{F_{dike} \cdot H_{dike}}{Hc} \cdot 100\%, \quad [9]$$

$$P_{LC} = 1 - P_{UC} = \frac{H_{AML}'}{H_{dike}} \cdot 100\%. \quad [10]$$

Taking the East Pacific Rise at 9°N as an example, where $U = 110$ km/My, $Hc = 6$ km, Z_{AML} (H_{dike}) = 1.5 km, and $F_{dike} = 1$, we get $\tau = 1.21$ kyr, $W_{dike} = 133$ m, $H_{AML}' = 150$ m, $P_{UC} = 25\%$, and $P_{LC} = 75\%$. In other words, dikes are modeled as 133-m wide intrusions at depths of 0–1.5 km every 1,210 years, accounting for 25% of the total melt flux. AML emplacements are 4-km wide and 150-m thick (H_{AML}') beneath the solidus isotherm every 1,210 years, accounting for 75% of the total melt flux.

However, at slow–ultraslow spreading ridges ($U \leq 40$ km/My), the solidus isotherm commonly lies beneath the crust ($Z_{AML} > Hc$ in Fig. 2*B*). If one assumes $F_{dike} = 1$, all melts have to be treated as dike intrusions that cut through the entire crust (i.e., forcing $H_{dike} = Hc$ and $P_{UC} = 100\%$), with no AML emplacement (i.e., $H_{AML}' = 0$ m and $P_{LC} = 0$; see the simulation with $U = 14$ km/My and $Hc = 6$ km in Fig. 2*H*). In other words, the crust is only built by dikes, which is unrealistic.

To better describe the diversity of MOR thermal regimes, and to account for the fact that plate separation at slow–ultraslow ridges is not fully accommodated by dikes, but also by faults, our model allows values of F_{dike} between 0 and 1. If the solidus isotherm lies at crustal depths (i.e., $Z_{AML} < Hc$), we use a similar treatment for dike intrusions and AML emplacements as standard models, but scale the dike width (W_{dike}) by F_{dike} (2) and adjust the AML thickness (H_{AML}') accordingly (8). If the solidus isotherm is below the crust (i.e., $Z_{AML} > Hc$) (e.g., Fig. 2*B*), dike injections cut through the entire crust, but $P_{UC} < 100\%$, so that AML emplacements still occur beneath the solidus isotherm. In this situation, dikes only lie at crustal depths with no connections to AMLs, and AMLs do not crystallize in the crust but in the mantle. This treatment enables us to simulate all possible spreading rates and crustal thicknesses in our model, and there is no cut-off of the AML depth at a certain spreading rate as in standard models (4, 5) (Fig. 3*D* and *SI Appendix*, Fig. S3*B*).

We assume that dikes have the same heat properties as AMLs and reset the temperature in the dike domain to be T_M during every intrusion event. As the model is discretized as 100 m × 100 m cells, we scale the latent and specific heat of the dike and the AML by geometric factors. For example, to intrude a 133-m-wide, 1.5-km-high dike (in the case of the EPR 9°N), we reset the temperature within a 2 × 15 matrix of cells (100 × 100 m for each) and scale its overall heat output by 133/200.

Comparing with Standard Models. We compare our predictions of AML depths using Hc = 6 km and F_{dike} = 1 (Fig. 3*A*) against the standard models based on enhanced diffusivity by Phipps Morgan and Chen (4) and coupled hydrothermal convection by Theissen-Krah et al. (5). The hydrothermal system of Phipps Morgan and Chen (4) is confined above Z_{cutoff} = 6 km with a cut-off temperature of T_{cutoff} = 600 °C and a Nusselt number of Nu = 8. The Nusselt number is a multiplier of thermal conductivity that enhances heat extraction within the permeable domain. The curve in Fig. 3*A* by Phipps Morgan and Chen (4) shows a relatively sharper drop in AML depths, compared to our model with Hc = 6 km and F_{dike} = 1, at spreading rates of <60 km/My. This is probably because of a different parameterization for the depth and temperature range where hydrothermal circulation is possible. Our model assumes that for the fluids to permeate deeper, the lithosphere must be colder, mimicking the dynamics of a cracking front (ref. 7 and see figure 2A and equation (3) in ref. 27). By contrast, Phipps Morgan and Chen (4) assumed sharper cutoffs in both temperature (<600 °C) and depth (<6 km). As a consequence, their modeled hydrothermal system may be more efficient at extracting heat at slow/ultraslow spreading ridges than ours. Both models however behave similarly at faster spreading rates, where the hotter thermal regime confines the permeable zone to shallower depths.

The hydrothermal convection model by Theissen-Krah et al. (5) uses the same limits on hydrothermal fluid depth and temperature as Phipps Morgan and Chen (4). However, it also assumes an axial permeability that decays exponentially with depth (y):

$$k = k_0 \exp(c \cdot y), \qquad [11]$$

where k_0 is the surface permeability at 4×10^{-15} m^2 and c is the decay constant at 8×10^{-4} m^{-1} (5). Our coupled hydrothermal convection model is empirically adjusted to fit the AML depth predictions of standard models (Fig. 3*A* and *SI Appendix*, Fig. S2): This is achieved for a uniform permeability of $k = 1 \times 10^{-15}$ m^2 and a maximum potential depth extent of Z_{H0} = 5 km. This uniform permeability is close to the depth-averaged permeability in the models of Theissen-Krah et al. (5): 1.5×10^{-15} m^2 and 1×10^{-15} m^2, respectively, for 3- and 5-km deep hydrothermal systems.

We further compare our steady-state models against the Nusselt number parameterization by Phipps Morgan and Chen (4), which varies Hc for U = 100, 60, and 20 km/My (*SI Appendix*, Fig. S2*A*). For U = 100 and 60 km/My, the solidus depths predicted by our hydrothermal model are comparable to the standard model. However, for U = 20 km/My, the solidus depths predicted by our model are overall shallower than the standard model (*SI Appendix*, Fig. S3*A*). This difference derives from the simplification of the hydrothermal cooling effect in the standard model that applies a constant Nusselt number (Nu = 8) to all simulations. If Nu = 8 is suitable for U = 100 and 60 km/My, a lower Nusselt number should probably be applied to U = 20 km/My, because the conductive boundary layer, between the base of the hydrothermal domain and the AML, is thicker at U = 20 km/My, resulting in overall less efficient hydrothermal cooling. We further run two groups of simulations with F_{dike} = 0 and F_{dike} = 0.5, using the same combinations of spreading rate and crustal thickness as in simulations with F_{dike} = 1 (*SI Appendix*, Fig. S3*B*). These simulations again show that the thermal effect of F_{dike} is low or negligible at the high melt fluxes of intermediate to fast spreading ridges but high at the lower melt fluxes of slow–ultraslow ridges.

Data, Materials, and Software Availability. The MATLAB script, modeling code, movies, and input files of all simulations, and an example for simulating the EPR 9°N are available on figshare (https://doi.org/10.6084/m9.figshare.21506217) (56).

ACKNOWLEDGMENTS. This work was supported by ANR project "Ridge Factory Slow" (ANR-18-CE01-0002-01). This is IPGP contribution #4245.

1. W. R. Buck, L. L. Lavier, A. N. B. Poliakov, Modes of faulting at mid-ocean ridges. *Nature* **434**, 719–723 (2005).
2. M. Cannat *et al.*, On spreading modes and magma supply at slow and ultraslow mid-ocean ridges. *Earth Planet. Sci. Lett.* **519**, 223–233 (2019).
3. M. D. Behn, G. Ito, Magmatic and tectonic extension at mid-ocean ridges: 1. Controls on fault characteristics. *Geochem., Geophys. Geosyst.* **9**, 8–10 (2008).
4. J. Phipps Morgan, Y. J. Chen, Dependence of ridge-axis morphology on magma supply and spreading rate. *Nature* **364**, 706–708 (1993).
5. S. Theissen-Krah, K. Iyer, L. H. Rüpke, J. P. Morgan, Coupled mechanical and hydrothermal modeling of crustal accretion at intermediate to fast spreading ridges. *Earth Planet. Sci. Lett.* **311**, 275–286 (2011).
6. F. J. Fontaine, J.-A. Olive, M. Cannat, J. Escartin, T. Perol, Hydrothermally-induced melt lens cooling and segmentation along the axis of fast- and intermediate-spreading centers. *Geophys. Res. Lett.* **38**, L14307 (2011).
7. J. A. Olive, T. J. Crone, Smoke without fire: How long can thermal cracking sustain hydrothermal circulation in the absence of magmatic heat? *J. Geophys. Res. Solid Earth* **123**, 4561–4581 (2018).
8. J. M. Sinton, R. S. Detrick, Mid-ocean ridge magma chambers. *J. Geophys. Res.* **97**, 197–216 (1992).
9. R. A. Dunn, D. R. Toomey, S. C. Solomon, Three-dimensional seismic structure and physical properties of the crust and shallow mantle beneath the East Pacific Rise at 9°30′N. *J. Geophys. Res. Solid Earth* **105**, 23537–23555 (2000).
10. A. F. Arnulf, A. J. Harding, G. M. Kent, W. S. D. Wilcock, Structure, seismicity, and accretionary processes at the hot spot-influenced axial seamount on the Juan de Fuca Ridge. *J. Geophys. Res. Solid Earth* **123**, 4618–4646 (2018).
11. S. C. Singh *et al.*, Discovery of a magma chamber and faults beneath a Mid-Atlantic Ridge hydrothermal field. *Nature* **442**, 1029–1032 (2006).
12. R. A. Dunn, V. Lekić, R. S. Detrick, D. R. Toomey, Three-dimensional seismic structure of the Mid-Atlantic Ridge (35°N): Evidence for focused melt supply and lower crustal dike injection. *J. Geophys. Res. Solid Earth* **110**, 1–17 (2005).
13. H. Jian *et al.*, Seismic structure and magmatic construction of crust at the ultraslow-spreading Southwest Indian Ridge at 50°28′E. *J. Geophys. Res. Solid Earth* **122**, 18–42 (2017).
14. J. Li *et al.*, Seismic observation of an extremely magmatic accretion at the ultraslow spreading Southwest Indian Ridge. *Geophys. Res. Lett.* **42**, 2656–2663 (2015).
15. L. Planert, E. R. Flueh, T. J. Reston, Along- and across-axis variations in crustal thickness and structure at the Mid-Atlantic Ridge at 5°S obtained from wide-angle seismic tomography: Implications for ridge segmentation. *J. Geophys. Res.* **114**, B09102 (2009).
16. D. A. Navin, C. Peirce, M. C. Sinha, The RAMESSES experiment–II. Evidence for accumulated melt beneath a slow spreading ridge from wide-angle refraction and multichannel reflection seismic profiles. *Geophys. J. Int.* **135**, 746–772 (1998).
17. M. C. Sinha *et al.*, Magmatic processes at slow spreading ridges: Implications of the RAMESSES experiment at 57°45′N on the Mid-Atlantic Ridge. *Geophys. J. Int.* **135**, 731–745 (1998).
18. C. Peirce, M. Sinha, S. Topping, C. Gill, Morphology and genesis of slow-spreading ridges-seabed scattering and seismic imaging within the oceanic crust. *Geophys. J. Int.* **168**, 59–89 (2007).
19. T. Seher *et al.*, Crustal velocity structure of the Lucky Strike segment of the Mid-Atlantic Ridge at 37°N from seismic refraction measurements. *J. Geophys. Res.* **115**, B03103 (2010).
20. J. Chen, W. C. Crawford, M. Cannat, Microseismicity and lithosphere thickness at a nearly-amagmatic oceanic detachment fault system. *Nat. Commun.* **14**, 430 (2023).
21. I. Grevemeyer *et al.*, Constraining the maximum depth of brittle deformation at slow-and ultraslow-spreading ridges using microseismicity. *Geology* **47**, 1069–1073 (2019).
22. M. Meier *et al.*, Segment-scale seismicity of the ultraslow spreading Knipovich Ridge. *Geochem., Geophys. Geosyst.* **22**, e2020GC009375 (2021).
23. J. Chen, T. Zhang, M. Tominaga, J. Escartin, R. Kang, Ocean sciences with the spilhaus projection: A seamless ocean map for spatial data recognition. *Sci. Data* **10**, 410 (2023).
24. Z. Liu, W. R. Buck, The spreading rate dependence of the distribution of axial magma lenses along mid-ocean ridges. *Proc. Natl. Acad. Sci. U.S.A.* **120**, e2214048120 (2023).
25. G. L. Christeson, J. A. Goff, R. S. Reece, Synthesis of oceanic crustal structure from two-dimensional seismic profiles. *Rev. Geophys.* **57**, 504–529 (2019).
26. Q. Fan, J. Olive, M. Cannat, Thermo-mechanical state of ultraslow-spreading ridges with a transient magma supply. *J. Geophys. Res. Solid Earth* **126**, e2020JB020557 (2021).
27. J. Chen, J. A. Olive, M. Cannat, Thermal regime of slow and ultraslow spreading ridges controlled by melt supply and modes of emplacement. *J. Geophys. Res. Solid Earth* **127**, e2021JB023715 (2022).
28. J. Chen, M. Cannat, C. Tao, D. Sauter, M. Munschy, 780 thousand years of upper-crustal construction at a melt-rich segment of the ultraslow spreading Southwest Indian Ridge 50 28′E. *J. Geophys. Res. Solid Earth* **126**, e2021JB022152 (2021).
29. J. P. Morgan, E. M. Parmentier, Crenulated seafloor: Evidence for spreading-rate dependent structure of mantle upwelling and melting beneath a mid-oceanic spreading center. *Earth Planet. Sci. Lett.* **129**, 73–84 (1995).
30. D. Sauter *et al.*, Continuous exhumation of mantle-derived rocks at the Southwest Indian Ridge for 11 million years. *Nat. Geosci.* **6**, 314–320 (2013).
31. M. West, W. Menke, M. Tolstoy, Focused magma supply at the intersection of the Cobb hotspot and the Juan de Fuca ridge. *Geophys. Res. Lett.* **30**, 1724 (2003).
32. P. A. Cowie, A. Malinverno, W. B. F. Ryan, M. H. Edwards, Quantitative fault studies on the East Pacific Rise: A comparison of sonar imaging techniques. *J. Geophys. Res.* **99**, 15205 (1994).
33. J. Escartín *et al.*, Interplay between faults and lava flows in construction of the upper oceanic crust: The East Pacific Rise crest 9°25′–9°58′N. *Geochem., Geophys. Geosyst.* **8**, Q06005 (2007).
34. J. A. Olive, P. Dublanchet, Controls on the magmatic fraction of extension at mid-ocean ridges. *Earth Planet. Sci. Lett.* **549**, 116541 (2020).
35. J. Phipps Morgan, Y. J. Chen, The genesis of oceanic crust: Magma injection, hydrothermal circulation, and crustal flow. *J. Geophys. Res. Solid Earth* **98**, 6283–6297 (1993).
36. V. Combier *et al.*, Three-dimensional geometry of axial magma chamber roof and faults at Lucky Strike volcano on the Mid-Atlantic Ridge. *J. Geophys. Res. Solid Earth* **120**, 5379–5400 (2015).
37. A. S. M. Cherkaoui, W. S. D. Wilcock, R. A. Dunn, D. R. Toomey, A numerical model of hydrothermal cooling and crustal accretion at a fast spreading mid-ocean ridge. *Geochem., Geophys. Geosyst.* **4**, 8616 (2003).

38. T. Barreyre, J. A. Olive, T. J. Crone, R. A. Sohn, Depth-dependent permeability and heat output at basalt-hosted hydrothermal systems across mid-ocean ridge spreading rates. *Geochem., Geophys. Geosyst.* **19**, 1259–1281 (2018).
39. W. C. Crawford *et al.*, Hydrothermal seismicity beneath the summit of Lucky Strike volcano, Mid-Atlantic Ridge. *Earth Planet. Sci. Lett.* **373**, 118–128 (2013).
40. M. Klischies, S. Petersen, C. W. Devey, Geological mapping of the Menez Gwen segment at 37°50′N on the Mid-Atlantic Ridge: Implications for accretion mechanisms and associated hydrothermal activity at slow-spreading mid-ocean ridges. *Mar. Geol.* **412**, 107–122 (2019).
41. W. J. Shinevar *et al.*, Causes of oceanic crustal thickness oscillations along a 74-M Mid-Atlantic Ridge flow line. *Geochem., Geophys. Geosyst.* **20**, 6123–6139 (2019).
42. C. Cordier *et al.*, Time scales of melt extraction revealed by distribution of lava composition across a ridge axis. *Geochem., Geophys. Geosyst.* **11**, Q0AC06 (2010).
43. H. Jian, S. C. Singh, Y. J. Chen, J. Li, Evidence of an axial magma chamber beneath the ultraslowspreading Southwest Indian Ridge. *Geology* **45**, 143–146 (2017).
44. V. Mendel *et al.*, Magmato-tectonic cyclicity at the ultra-slow spreading Southwest Indian Ridge: Evidence from variations of axial volcanic ridge morphology and abyssal hills pattern. *Geochem., Geophys. Geosyst.* **4**, 9102 (2003).
45. S. J. Sim, Persistent magma-rich waves beneath mid-ocean ridges explain long periodicity on ocean floor fabric. *Geophys. Res. Lett.* **49**, e2022GL098110 (2022).
46. C. R. German, L. M. Parson, Distributions of hydrothermal activity along the Mid-Atlantic Ridge: Interplay of magmatic and tectonic controls. *Earth Planet. Sci. Lett.* **160**, 327–341 (1998).
47. Y. J. Chen, Influence of the Iceland mantle plume on crustal accretion at the inflated Reykjanes Ridge: Magma lens and low hydrothermal activity? *J. Geophys. Res.* **108**, 2524 (2003).
48. J. Escartin *et al.*, Hydrothermal activity along the slow-spreading Lucky Strike ridge segment (Mid-Atlantic Ridge): Distribution, heatflux, and geological controls. *Earth Planet. Sci. Lett.* **431**, 173–185 (2015).
49. R. S. White, J. W. Bown, J. R. Smallwood, The temperature of the Iceland plume and origin of outward-propagating V-shaped ridges. *J. Geol. Soc. London.* **152**, 1039–1045 (1995).
50. J. Lin, G. M. Purdy, H. Schouten, J.-C. Sempere, C. Zervas, Evidence from gravity data for focused magmatic accretion along the Mid-Atlantic Ridge. *Nature* **344**, 627–632 (1990).
51. M. Cannat, How thick is the magmatic crust at slow spreading oceanic ridges? *J. Geophys. Res. Solid Earth* **101**, 2847–2857 (1996).
52. J. Chen *et al.*, Evolution of enhanced magmatism at the ultraslow spreading Southwest Indian Ridge between 46°E and 53.5°E. *Tectonophysics* **860**, 229903 (2023).
53. J. J. Standish, H. J. B. Dick, P. J. Michael, W. G. Melson, T. O'Hearn, MORB generation beneath the ultraslow spreading Southwest Indian Ridge (9–25°E): Major element chemistry and the importance of process versus source. *Geochem., Geophys. Geosyst.* **9**, Q05004 (2008).
54. M. Cannat, Emplacement of mantle rocks in the seafloor at mid-ocean ridges. *J. Geophys. Res. Solid Earth* **98**, 4163–4172 (1993).
55. M. Spiegelman, D. McKenzie, Simple 2-D models for melt extraction at mid-ocean ridges and island arcs. *Earth Planet. Sci. Lett.* **83**, 137–152 (1987).
56. J. Chen, J. A. Olive, M. Cannat, Research Data for 'Beyond spreading rate: controls on the thermal regime of mid-ocean ridges'. Figshare. https://doi.org/10.6084/m9.figshare.21506217. Deposited 8 August 2023.